**ORIGINAL ARTICLE**

# A physics-based algorithm for real-time simulation of electrosurgery procedures in minimally invasive surgery

Zhonghua Lu[1]
Venkata S. Arikatla[2]
Zhongqing Han[2]
Brian F. Allen[2]
Suvranu De[2]*

[1]*Intelligent Manufacture and Control Institution, Wuhan University of Technology, People's Republic of China*

[2]*Department of Mechanical, Aerospace and Nuclear Engineering, Rensselaer Polytechnic Institute, Troy, NY, USA*

*Correspondence to: Suvranu De, JEC 2052, Department of Mechanical, Aerospace and Nuclear Engineering, Director, Center for Modeling, Simulation and Imaging in Medicine (CeMSIM), Rensselaer Polytechnic Institute (RPI), 110 Eighth Street, Troy, NY 12180, USA. E-mail: des@rpi.edu

## Abstract

**Background**   High-frequency electricity is used in the majority of surgical interventions. However, modern computer-based training and simulation systems rely on physically unrealistic models that fail to capture the interplay of the electrical, mechanical and thermal properties of biological tissue.

**Methods**   We present a real-time and physically realistic simulation of electrosurgery by modelling the electrical, thermal and mechanical properties as three iteratively solved finite element models. To provide subfinite-element graphical rendering of vaporized tissue, a dual-mesh dynamic triangulation algorithm based on isotherms is proposed. The block compressed row storage (BCRS) structure is shown to be critical in allowing computationally efficient changes in the tissue topology due to vaporization.

**Results**   We have demonstrated our physics-based electrosurgery cutting algorithm through various examples. Our matrix manipulation algorithms designed for topology changes have shown low computational cost.

**Conclusions**   Our simulator offers substantially greater physical fidelity compared to previous simulators that use simple geometry-based heat characterization. Copyright © 2013 John Wiley & Sons, Ltd.

**Keywords**   physics-based simulation; electrosurgery; minimally invasive surgery; virtual reality; surgical simulation; cutting simulation

## Introduction

Electrosurgical devices are used in the majority of surgical procedures today (1). These devices generate a high-frequency (300–700 kHz) and high power-density electric current through the tissue, heating the tissue directly (2). An expert surgeon can precisely control the heating effect to burn tissue locally while minimizing inadvertent thermal damage and blood loss. Limiting the thermal spread is a key surgical skill, yet current hands-on approaches to teaching electro-surgery have severe drawbacks. *In vivo* animal models provide the highest fidelity, but are expensive for basic skills training. *Ex vivo* tissue models are unable to model blood flow effects and generate carcinogenic smoke (3). Computer simulation of electrosurgery promises low cost, safe and flexible training (4). However, previously proposed systems have limited physical fidelity, relying on geometric and graphical means of estimating and communicating tissue effects. A barrier to improved physical realism is that the thermal, electrical

and viscoelastic states of the simulated tissue are interdependent, greatly increasing the implementation and computational complexity.

In this paper, we propose a novel approach to simulating the effects of external forces and electrical current on tissue. We focus on tissue cutting through vaporization, an important skill for safe and effective practice (1). Our approach is based on a finite-element electro–thermo–elastic analysis of the biological tissue. A volumetric tetrahedral mesh simulates the elastic deformation with a linear, co-rotational finite element model (FEM) (5). The electrical current and temperature are similarly modelled using linear FEMs. Deformation can be decoupled from the thermal and electrical models because vaporization takes place at time scales that are much faster compared to the timescales on which the tissue parameters change due to thermal or electrical effects. However, the thermal and electrical models have similar time scales and therefore must be coupled for accurate results.

We introduce a novel dual-mesh algorithm, with a coarse tetrahedral volumetric mesh for physics computation and a detailed surface mesh for isotherm-based visual rendering, for rendering partially vaporized tissue at spatial resolutions much finer than the underlying tetrahedral mesh. An isothermal surface that represents the extent of vaporization is interpolated from the thermal model. The isothermal surface is dynamically calculated for each time step and forms the visible tissue geometry. This approach provides greatly increased visual resolution of the thermal effects, yet remains physically accurate.

A difficult problem for FEM of surgery is topological changes, such as from cutting (6). Our approach relies on online manipulation of the matrix data structure to achieve cutting through vaporization in real time.

To achieve high-quality, physically realistic electrosurgical simulation capable of real-time rates on modest hardware, this study introduces: (a) a method for coupled thermo-electrical FEM combined with an elastic deformation FEM; (b) an electrosurgical cutting model based on tissue vaporization; (c) a novel method for rendering subtetrahedron tissue surfaces, using the isothermal surface; and (d) the online manipulation of the matrix data structures.

In spite of its importance in surgery, the literature on modelling of electrosurgery procedures is surprisingly limited. Dodde *et al*. (7) used a coupled thermal-electric FEM formulation to analyse temperature-dependent electrical and thermal properties for the tissue. Although the physics of electrosurgical procedures is analysed in this paper, the simulations are performed off-line and real-time interaction and rendering is not considered. Maciel *et al*. (8) simulated an electrosurgery process on a three-dimensional (3D) domain using a mass-spring model in real time. However, mass-spring systems can be unstable and require many sensitive parameters. Furthermore, even arbitrarily dense mass-spring meshes may not converge to the solution of the underlying partial differential equation. In Lu *et al*. (9), a commercial physics engine, PhysX™, was used for physics-based deformation and the

electrical heat source was modelled as a simple spherical distribution. In (10), Lu *et al*. modelled the heat conduction and deformation combined with the cutting model to achieve real-time interactive electrocautery simulation. We have extended this method to include modelling of electric potential using finite elements.

Developing computational models for electrosurgery procedures requires investigation of tissue properties. Tissue deformation and force feedback during monopolar electrosurgery procedures have been measured. Jacob *et al*. (11) estimated the critical temperatures for cutting tissues of various organs. A physics-driven neural networks-based simulation system was shown to be capable of simulating the response of non-linear deformable objects in real time (12); however, this approach cannot be easily extended to changing topology, e.g. cutting, or to dynamic interactions.

While models of electrosurgical cutting are rare, surgical cutting in general has been extensively investigated. Cutting algorithms can be broadly classified into two categories. In the first category of algorithms, the existing geometry is manipulated by either splitting the shared vertices (9) or removing them (13). In the second category, new geometry is created by remeshing along the cut. Remeshing involves either connecting new vertices or subdividing existing elements. After multiple cuts, the number of newly generated elements might be prohibitively high using this method. In (14), a cutting simulation using tetrahedral elements was proposed, using a hybrid approach that combines both the above methods.

All previous cutting algorithms targeting surgery simulation use a scalpel. However, during electrosurgery procedures, the cut is initiated by the high-frequency current, which heats the tissue, ultimately vaporizing it. This phenomenon is predominantly a heat-transfer process taking place in the vicinity of the tool tip, causing the temperature to rise locally to about 400–600°C (15). To the best of our knowledge, no previous study has accounted for this temperature rise as the determinant of the cutting process in electrosurgery procedures.

# Materials and methods

## Numerical modelling of the electrosurgery process

The interaction of the electrosurgical tool with soft tissue results in the deformation of the tissue, localized heating and corresponding force feedback to the tool. In the next section, we present the relevant equations of linear elastodynamics and their finite element discretization, with the the thermo-electric FEM formulation in the following section. A co-rotational formulation is used to account for large non-linear rotations of the organs due to manipulation by the surgical tools. Time integration schemes are presented in the section after that.

## Linear elastodynamics

The elasticity model is based on linear continuum elasticity theory (27). We use the finite element method with linear displacement tetrahedral to solve the governing equation (21). Then the displacement field is discretized as:

$$\mathbf{u}(\mathbf{x},t) = \mathbf{N}(\mathbf{x})\mathbf{U}(t) = \sum_e \mathbf{N}_e(\mathbf{x})\mathbf{U}_e(t) \quad (1)$$

where $\mathbf{N}_e(\mathbf{x})$ is a $3 \times 12$ matrix that contains the shape functions of the tetrahedral element and $\mathbf{U}_e(t) = [u_1, v_1, w_1, \ldots, u_4, v_4, w_4]^T$ is nodal point displacement vector (16). Hence, the discretized problem corresponding to equation (6) is:

$$\mathbf{M}\ddot{\mathbf{U}} + \mathbf{C}\dot{\mathbf{U}} + \mathbf{K}\mathbf{U} = \mathbf{F} \quad (2)$$

subject to:

$$\mathbf{U}_e(t) = 0 \quad \text{on} \quad \Gamma_u \times (0, \tau) \quad (3)$$

$$\mathbf{U}_e(t = 0) = \mathbf{U}_e^0 \quad \mathbf{x} \in \Omega \quad (4)$$

$$\dot{\mathbf{U}}_e(t = 0) = \mathbf{U}_e^0 \quad \mathbf{x} \in \Omega \quad (5)$$

where $\mathbf{M}$ is the global mass matrix assembled using element consistent mass matrices $\mathbf{M}_e = \int_{V_e} \rho \mathbf{N}_e^T \mathbf{N}_e dV$, $\mathbf{C}$ is the viscous Rayleigh damping matrix, with $\mathbf{C} = \alpha \mathbf{M} + \beta \mathbf{K}$ $\alpha$ and $\beta$ being the damping constants (17), and $\mathbf{K}$ is the global stiffness matrix, assembled using element stiffness matrices $\mathbf{K}_e = \int_{V_e} \mathbf{B}_e^T \mathbf{E} \mathbf{B}_e dV$, where $\mathbf{E}$ is a $6 \times 6$ elasticity matrix which, for isotropic materials, depends on two scalars – the Young's modulus and the Poisson's ratio – and the strain–displacement matrix $\mathbf{B}_e = \nabla \mathbf{N}_e$ can be precomputed for every tetrahedron, and $\mathbf{F}_e = \int_{V_e} \mathbf{f} \cdot \mathbf{N}_e dV + \int_{\Gamma_e} \mathbf{h} \cdot \mathbf{N}_e d\Gamma$ is the vector of external nodal point forces, where $\mathbf{f}$ is the vector of body forces and $\mathbf{h}$ is the vector of natural boundary conditions.

To account for large rotations, the stiffness matrix and force vector are corrected using the co-rotational framework (5,18):

$$\overline{\mathbf{K}}_e = \mathbf{R}_e \mathbf{K}_e \mathbf{R}_e^T \quad (6)$$

$$\overline{\mathbf{F}}_e = \mathbf{F}_e - \mathbf{R}_e \mathbf{K}_e \mathbf{x}_e^0 \quad (7)$$

where $\mathbf{R}_e$ is the element rotation matrix with respect to the element's barycentre, $\mathbf{x}_e^0$ is the nodal coordinate vector of the element in initial configuration ($t = 0$), and $\mathbf{F}_e$ is the elemental internal force vector. These elemental force vectors are assembled at each time step. The element-wise rotations are computed using polar decomposition.

## Thermo-electric FEM formulation

During electrosurgery, alternating current is used to directly heat the tissue, while the probe tip remains relatively cool. The temperature distribution $T(\mathbf{x}, t)$ in the tissue is governed by the following bio-heat differential equation (19):

$$\rho c \frac{\partial T}{\partial t} = k \nabla^2 T + w_b c_b (T - T_a) + q_m + q_g \quad in \ \Omega \quad (8)$$
$$\times (0, \tau)$$

where $\nabla^2 = \partial^2 / \partial u_1^2 + \partial^2 / \partial u_2^2 + \partial^2 / \partial u_3^2$ is the Laplace

operator, $k$ is the thermal conductivity of the tissue, $w_b$ is the effective blood perfusion parameter, $c_b$ is the blood heat capacity, $T_a$ is the blood inlet temperature or steady-state temperature of the tissue, $q_m$ is the metabolic heat generation rate of the tissue, and $q_g$ is the externally induced heat generation rate due to electrosurgical heating. In this study, $q_m$ and $w_b$ are both assumed to be negligible, as the energy input into the tissue is much greater than that produced during metabolism, and compression of the tissue from the electrode inhibits local blood flow. Hence, equation (8) can be written as:

$$\rho c \frac{\partial T}{\partial t} = k \nabla^2 T + q_g(\mathbf{x}) \ \text{on} \ \Omega \times (0, \tau) \quad (9)$$

At the frequencies employed and within the area of interest, the tissues can be considered purely resistive, because the displacement currents are negligible. For this reason, a quasi-static approach is usually employed to resolve the electrical problem. The distributed heat source, $q_g$, is given by:

$$q_g = J \cdot E \quad (10)$$

where $J$ is the current density (A/m$^2$) and E is the electric field intensity (V/m). These two vectors are evaluated using Laplace's equation (20):

$$\nabla \cdot (\sigma \nabla V) = 0 \quad (11)$$

where $V$ is the potential (V) and $\sigma$ is the electrical conductivity (S/m). Assuming that the electrical conductivity is constant, Laplace's equation can be solved independently. The electric potential can be solved efficiently over the entire volume and the solution can be implemented into the source term of the heat conduction equation.

As the effect of heat radiation is considered insignificant, the major boundary conditions are convective heat loss from the surface, $\Gamma_h$, of the organ, given by:

$$(k \nabla T) \cdot \mathbf{n} + h(T - T_a) = 0 \ for \ t > 0 \ on \ \Gamma_h \quad (12)$$

where $h$ is convection heat transfer coefficient, $T_a$ is the ambient temperature and $\mathbf{n}$ is the unit outward normal on the boundary. Then, the discretized problem corresponding to equation (9) is:

$$\mathbf{C}_T \cdot \dot{\mathbf{T}} + \mathbf{K}_T \cdot \mathbf{T} = \mathbf{Q} \quad (13)$$

where $\mathbf{C}_T$ is the heat capacity matrix, $\mathbf{K}_T$ is the heat conductivity matrix, $\mathbf{Q}$ is the heat supply vector, $\mathbf{T}$ is vector of nodal point temperatures, and $\dot{\mathbf{T}}$ is the time derivative of $\mathbf{T}$ with the following expressions:

$$\mathbf{C}_T = \int_{V_e} \rho c \mathbf{N}^T \cdot \mathbf{N} dV \quad (14)$$

$$\mathbf{K}_T = \int_{V_e} k(\nabla \mathbf{N})^T \cdot (\nabla \mathbf{N}) dV + \int_{\Gamma_h} h \mathbf{N}^T \cdot \mathbf{N} d\Gamma \quad (15)$$

$$\mathbf{Q} = \int_{V_e} \mathbf{q}_g \cdot \mathbf{N} dV \quad (16)$$

where $\mathbf{N}$ is the matrix of shape functions. Then, the electrical boundary conditions are insulating conditions (($\sigma \nabla V) \cdot \mathbf{n} = 0$), electric ground condition ($V = 0$) and energy input condition at the contacting area between the electrode and tissue ($V \neq 0$). Therefore, the discretized problem corresponding to equation (11) is:

$$\mathbf{K}_e \mathbf{V} = \mathbf{S} \qquad (17)$$

where $\mathbf{K}_e = \int_{V_e} \sigma (\nabla \mathbf{N})^T \cdot (\nabla \mathbf{N}) dV$ , $\mathbf{S} = \int_{\Gamma_h} (\sigma \mathbf{N} \cdot \nabla V) \cdot \mathbf{n} d\Gamma$.

Then, we can use the equation $\mathbf{q}_g = \mathbf{J} \cdot \mathbf{E} = \sigma (\nabla V)^2$ to get the source term of the heat conduction equation.

## Time integration

Time integration in equation (2) is performed using the Newmark-$\beta$ method (21). The resulting set of discretized equations is of the following form:

$$\mathbf{K}_{eff} \mathbf{U}(t + \Delta t) = \mathbf{F}_{eff}(t + \Delta t) \qquad (18)$$

where $\mathbf{K}_{eff} = \mathbf{K} + a_0 \mathbf{M} + a_1 \mathbf{C}$ is the effective stiffness matrix and $\mathbf{F}_{eff}(t + \Delta t) = \mathbf{F}(t) + \mathbf{M}\left[a_0 \mathbf{U}(t) + a_2 \dot{\mathbf{U}}(t) + a_3 \ddot{\mathbf{U}}(t)\right] + \mathbf{C}\left[a_1 \mathbf{U}(t) + a_4 \dot{\mathbf{U}}(t) + a_5 \ddot{\mathbf{U}}(t)\right]$ is the effective force vector ($a_0$–$a_5$ are Newmark constants).

For heat transfer equation (9), we use the following central difference scheme:

$$\dot{\mathbf{T}} = \frac{\mathbf{T}_1 - \mathbf{T}_0}{\Delta t} \qquad (19)$$

where $\mathbf{T}_1 = \mathbf{T}(t + (\Delta t/2))$, $\mathbf{T}_0 = \mathbf{T}(t - (\Delta t/2))$ and $\Delta t$ is the time step. The resulting set of equations to be solved at a given time step is:

$$\left(\mathbf{K}_T + \frac{2}{\Delta t}\mathbf{C}_T\right)\mathbf{T} = \frac{2}{\Delta t}\mathbf{C}_T \mathbf{T}_0 + \mathbf{Q} \qquad (20)$$

## Isotherm-based dual-mesh algorithm

An electrosurgical tool works by vaporizing nearby tissue. As the instrument tip moves through the tissue, the model must be updated at each time step. This amounts to locally remeshing and regenerating the global stiffness matrix at every time step, which is prohibitively expensive and would not allow real-time interactive simulation. Also, remeshing at every time step may result in irregular element shapes, which result in poor solution accuracy. The dual-mesh algorithm developed in this paper overcomes this problem by dynamically computing a surface mesh for graphical output. This visual surface is derived from the simulation's tetrahedral mesh and the temperature distribution. Portions of the finite element mesh that exceed a critical vaporization temperature ($T_v$) are visually removed from the visual surface. However, for physics-based computations, a finite element is not removed until all its nodes have temperatures in excess of $T_v$. The algorithm is first summarized below and then explained in detail.

### Isotherm definition

The first step is to define the $T_v$ isotherms. Assuming that $T_1$ and $T_2$ are the nodal temperatures on an element edge, if $T_1 < T_v$ and $T_2 > T_v$, then the isotherm intersects the edge at:

$$\mathbf{X}_c = \mathbf{X}_2 a + \mathbf{X}_1 (1 - a) \qquad (21)$$

where $\mathbf{X}_1$, $\mathbf{X}_2$ and $\mathbf{X}_c$ are the coordinates of the two end nodes and the intersecting node on the edge, $a = (T_v - T_1)/(T_2 - T_1)$.

For a tetrahedral finite element, the following four cases may occur:

- *Case 1*: temperatures of all four nodes are $\leq T_v$. In this case the element remains intact and is considered for both deformation and temperature computations.
- *Case 2*: temperatures of all four nodes are $\geq T_v$. In this case the element is removed from the mesh and not considered for deformation and temperature computations.
- *Case 3*: temperatures of one or three nodes exceed $T_v$. In this case the isotherm is represented by a plane defined by three points. The portion of the tetrahedron with temperature exceeding $T_v$ is removed for visual rendering only. The tetrahedron is, however, considered for both deformation and temperature computations. As shown in Figure 1, plane EFG represents the isotherm, and the tetrahedron AEFG is removed from the mesh for visual rendering purposes only.
- *Case 4*: temperatures of two nodes exceed $T_v$. In this case the isotherm is represented by a plane defined by four points. The portion of the tetrahedron with temperature exceeding $T_v$ is removed for visual rendering only. The tetrahedron is, however, considered for both deformation and temperature computations. As shown in Figure 2, plane EFGH represents the isotherm and the polyhedron ABEFGH is removed from the mesh for visual rendering purposes only.

As the electrosurgery tip moves away, due to conductive heat loss, some of the nodes will cool down to temperatures below $T_v$. However, the cutting procedure is irreversible. This is implemented by recording the highest temperature of every node in the electrosurgery process and using that temperature to define the final isotherm.

## Visual rendering

In our simulation, only the surface of the model is visually rendered. During initialization, each face of each tetrahedron is labelled as either a surface face or an interior face.
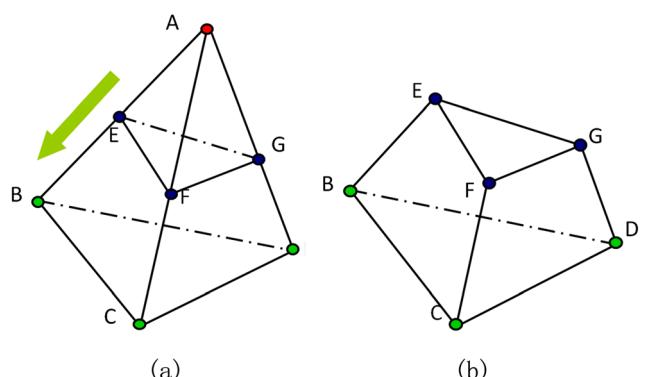


**Figure 1.** Case 3: (a) with the temperature of node A of the tetrahedral element exceeding the threshold temperature, resulting in (b) the visual surface EFG
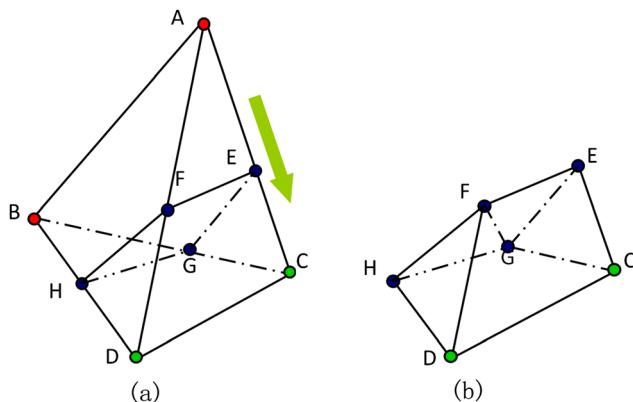
**Figure 2. Case 4: (a) with temperature of two nodes, A and B, exceeding the threshold temperature, resulting in (b) the visual surface EFGH**

If a tetrahedron is cut by the $T_v$ isotherm (shown as the purple contour in Figure 3a), new element faces are created and portions of the existing elements are removed, based on the algorithm described above. The new faces are added to the rendering buffer.

As mentioned above, a tetrahedron is not removed from the mesh until all its nodes have temperatures exceeding
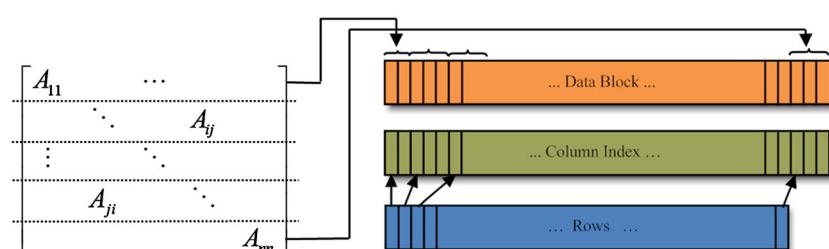


**Figure 3. A 2D illustration of splitting of nodes with temperatures greater than the threshold temperature (red) into (a) two nodes, each shown in (b). The direction of split is chosen based on the temperatures of neighbouring nodes (c, d)**

$T_v$. This may cause visual artifacts in rendering the deformation, as the mesh for deformation computation remains unchanged. To overcome this problem, we split the nodes along the normal to the plane defined by three nodes with the highest temperatures, as shown in Figure 3.

The dual-mesh algorithm enables us to consider the visual rendering and physical computation separately, and also the two procedures are conducted in different threads. Hence, although the mesh complexity dynamics during the rendering procedure will lead to a slight increase in time, due to the increase in the number of elements involved in the cuts (0.4–15 ms), it will not affect the subsequent physical computation. The mesh for physical simulation changes only when the temperatures at all nodes of a tetrahedron exceed the isotherm. Therefore, the accuracy and computational cost of physical simulation are determined by the size of the physical mesh itself.

## Fast matrix updates

During the electrosurgery process, new nodes are created by node splitting and nodes are removed when the temperature of all nodes of a single tetrahedron exceed the threshold. When a new node is added during splitting, some of the old connections must be deleted and connections to the new nodes created. Since each edge corresponds to a $3 \times 3$ block in the global stiffness matrix, the sparse structures have to be modified based on the nodal addition or deletion. Hence, a block-based storage structure is suitable for dealing with the nodal addition and deletion. Additionally, the block compressed row storage (BCRS) scheme exploits non-zero elements in contiguous locations by packing. If we know the column index of the first non-zero element in a block, then we also know the column indices of all the other non-zero elements. In other words, only one memory indirection is required for each block (22).

The FEM deformation matrices are block-sparse and we apply the block compressed row format storage, as shown in Figure 4. To store a sparse matrix K, we encode the non-zero entries and their respective column indices in two separate arrays in a row-wise fashion. Additionally, an index is stored for every row, which references the first non-zero entry in that row.

If the node is split, and if one edge linking nodes $i$ and $j$ ($i < j$) is deleted, then $3 \times 3$ blocks $A_{ij}$ and $A_{ji}$ need to be removed in the BCRS structure. So the size of data block
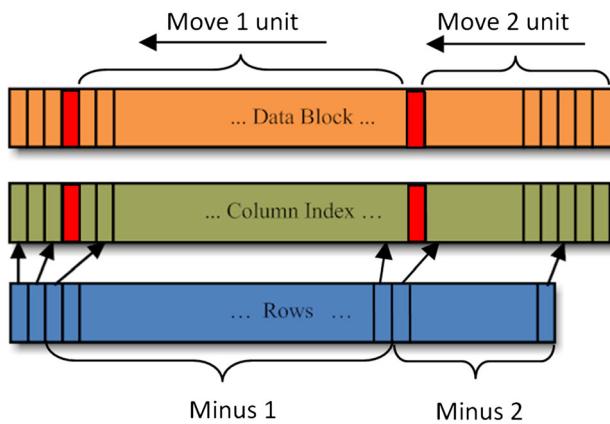


**Figure 4. Block compressed row storage scheme**

Figure 5. Scheme for deleting one edge

is −2, the same as the size of column index. As shown in Figure 5, the data block and column index move one unit between $A_{ij}$ and $A_{ji}$, two units after $A_{ji}$. Similarly, if a new edge is added, one has to expand the arrays to add an additional $3 \times 3$ block. As shown in Figure 6, in case a new node is created, the size of the global stiffness matrix is increased by 3 and the new row is filled according to the nodal connections (23).

Node splitting also creates a new node and its corresponding edges have to be established. First, a new row is appended in the BCRS structure and all the deleted connections of its parent node are established. The edges that the split nodes have are governed by the cutting plane, as shown in Figure 3.

In the thermo-electric coupled model, each node is associated with a single scalar variable; hence, a compressed row storage structure (CRS) is used. Only one non-zero value is added or deleted, according to the procedure described above.
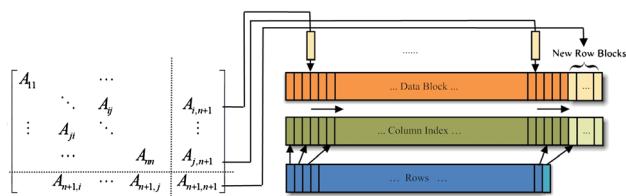


Figure 6. Matrix manipulations to add a new node

## Results

As our target is a low-cost simulator, performance is measured on modest hardware: an Intel Core 2 Quad Q9550 CPU and NVIDIA GTX 280 graphics processor. Two PHAN-ToM Omni haptic interface devices are used for input and force feedback and OpenGL is used as the graphic rendering environment. During the simulation, physics updates (including deformation, heat transfer, current density flow and node splitting) average around 50 Hz and graphics and haptics rendering are around 60 Hz and 1000 Hz, respectively. The electrosurgical tools are modelled based on real surgical tools in Autodesk 3DS Max software. Four execution threads are used, one each for isothermal rendering, collision detection, physics update and force rendering. Figure 7 shows an overview of the simulation.

In the present simulation we use the material properties as listed in Table 1. These properties are based on the study conducted by Carter and Doddle (7,24).

The effects of the dual-mesh algorithm based on isotherm rendering are shown in Figure 8. Note that the computationally expensive remeshing process is avoided, yet the displayed geometry shows fine details around the region of vaporization. This improved visual accuracy is physically correct, as it is derived from the temperature model. During training in surgical procedures, the physical fidelity of our simulator can enable trainees to obtain a near-realistic response by adjusting the energy input parameters. This is not possible with simulators that use simple geometry-based heat characterization. In addition, the mesh as shown in Figure 8c is used only for rendering

Table 1. The physical properties of tissue used in the simulation

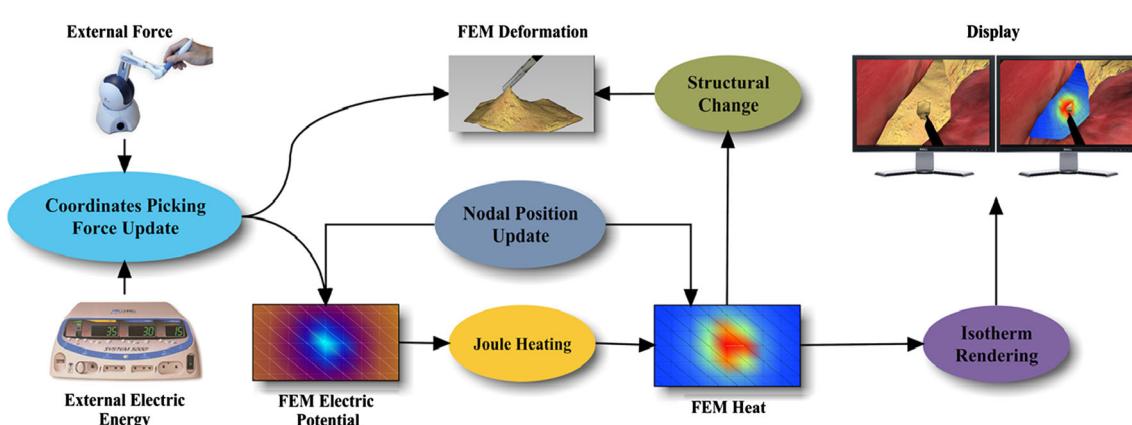| Parameter | Simulation value |
|---|---|
| Young's modulus (N/m$^2$) | $2.7 \times 10^5$ |
| Poisson's ratio | 0.4 |
| Thermal conductivity (W/m·K) | 0.512 |
| Density (kg/m$^3$) | 1060 |
| Specific heat (J/kg·K) | 3600 |
| Electrical conductivity (S/m) | 0.33 |



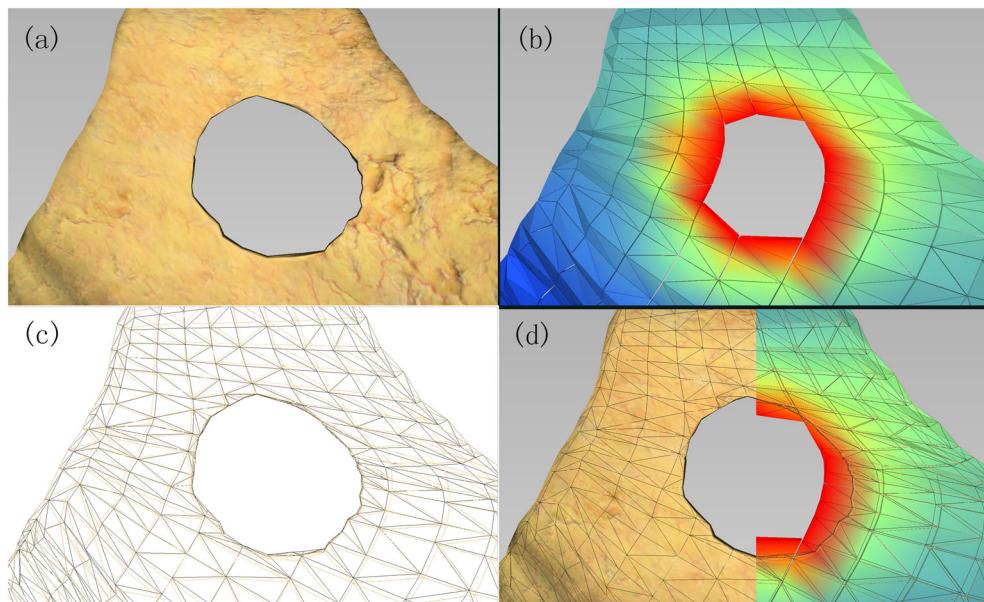Figure 7. Overview of the components of the overall simulation system

**Figure 8.** (a) Geometric rendering of the cut part of the tissue, based on isotherm (b) corresponding mesh for the underlying physics simulation; (c) mesh used for rendering, based on isotherm; and (d) comparison between the simulation mesh and the rendering mesh

purposes, while the mesh in Figure 8b is used for multi-physics computations. Thus, the very small elements or badly shaped elements (i.e. slivers) appearing in the vicinity of cuts of Figure 8c will not cause simulation slowdown or ill-conditioning and the element count will not dramatically increase, which is essential for real-time simulation.

Figure 9 shows the simulation results of multi-physics computation: deformation, electric potential distribution and temperature distribution, respectively.

Figure 10 shows an example tetrahedral mesh with 1022 nodes, representing a human liver. Table 2 provides the computational time required for each stage of simulation. The execution time for deformation, heat transfer
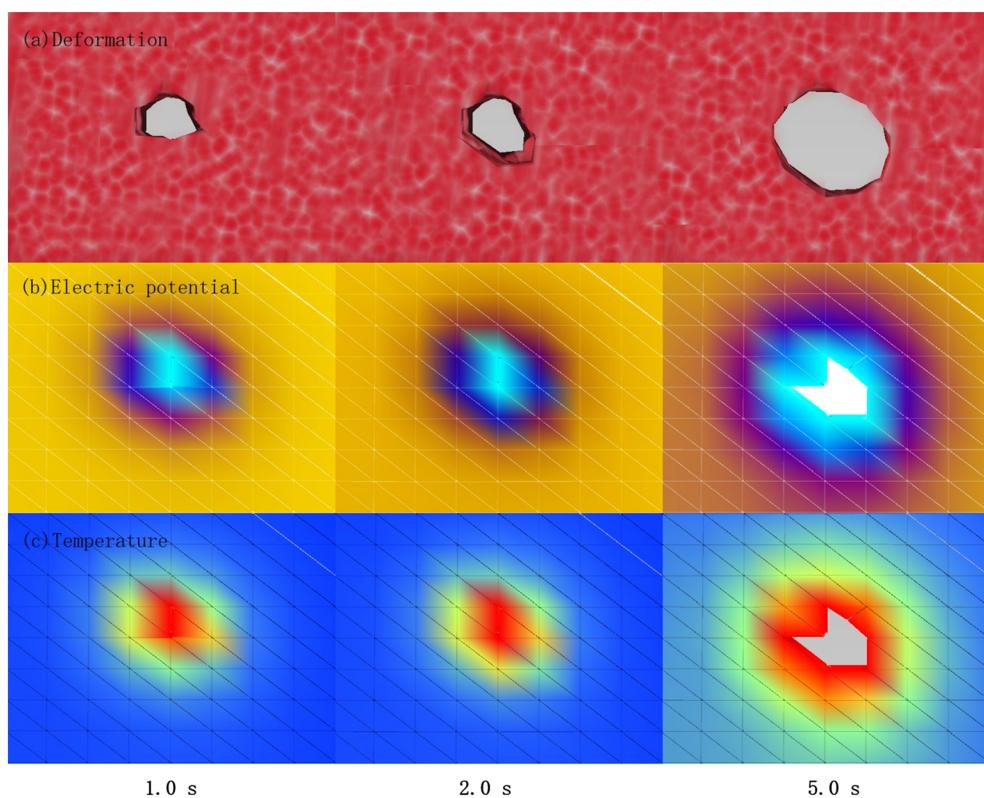


**Figure 9.** An example of progressive vaporization (left to right) due to a stationary electrosurgical instrument (not shown) on a thin tissue. Shown are the three finite element models: (a) deformation; (b) electric potential; and (c) temperature
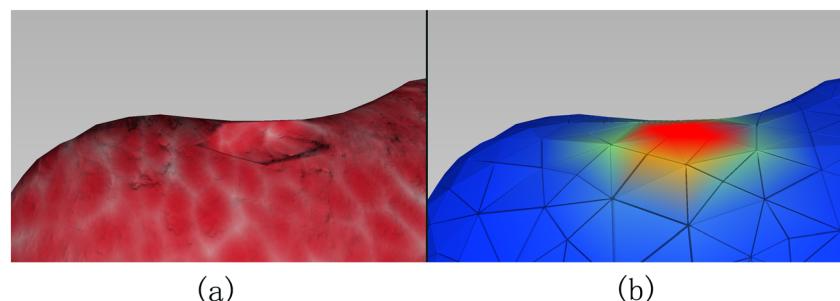
**Figure 10. (a) Visual rendering of the cauterized portion of the liver; (b) the underlying tetrahedral model, colour-mapped based on temperature**

**Table 2. Computational time of simulation components (liver mesh in Figure 10)**

| Process | Time (ms) |
| --- | --- |
| Deformation | 18–19 |
| Heat transfer | 1.5–1.6 |
| Current flow | 1.5–1.6 |
| Isotherm rendering | 0.4–15 |

and current flow are stable, while the time consumed in isotherm rendering is in the range 0.4–15 ms. This large variation in computational load is due to the varying number of tetrahedrons intersecting the isotherm. The isotherm rendering is conducted in a different thread.

Figure 11 shows the computation time in updating the deformation, nodal temperature and current density within each iteration. A preconditioned conjugate gradient iterative solver is used, with a tolerance of $10^{-6}$ for the deformation, temperature and current density updates. As expected, the deformation update requires more computation, as the degrees of freedom of the deformation model are three times those of the temperature or electrical models. Additionally, the co-rotational method is used in the deformation simulation in order to solve large non-linear rotations. This requires additional computation cost.

Cutting through vaporization is implemented using the algorithm described above. The main cost in cutting is associated with isotherm definition, nodal splitting and the resulting modification of the sparse structures. A comparison of the costs of rebuilding the sparse matrix directly vs using the BCRS method is shown in Figure 12. The comparison is made with respect to the mesh sizes, which are proportional to the array sizes in the BCRS. A speed-up of at least 270% is observed. In order to reach an update rate of 30 Hz for real-time graphics, the corresponding numbers of tetrahedrals of the two methods are about 1500 and 3450. Hence, more realistic and detailed cutting can be conducted using our method.

Figure 13 shows screenshots of a real-time simulation scenario for a virtual laparoscopic adjustable gastric banding (LAGB) surgical procedure. This is the mostly widely used procedure in the USA for achieving weight loss in a reversible manner (25).

# Discussion

In this paper we have presented an algorithm for real-time multiphysics-based interactive electrosurgical simulations, with a coarse tetrahedral volumetric mesh for computing deformations, current flow and temperature fields and a detailed surface mesh for isotherm-based visual rendering. To account for large rotations, a co-rotational deformation method is used. A block compressed row storage structure is used to solve the sparse matrices,
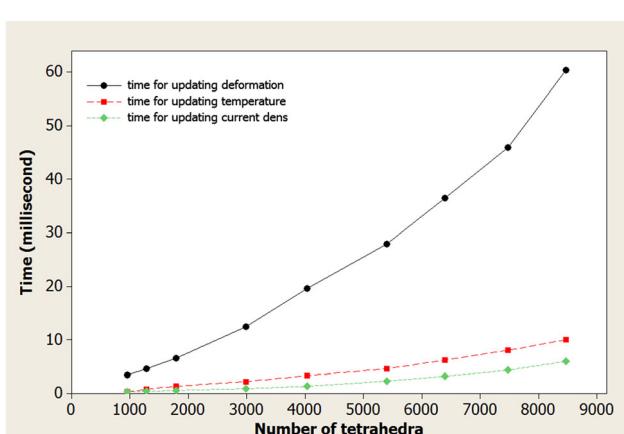


**Figure 11. Comparison of the execution time for updating the nodal displacement, temperature and current density**
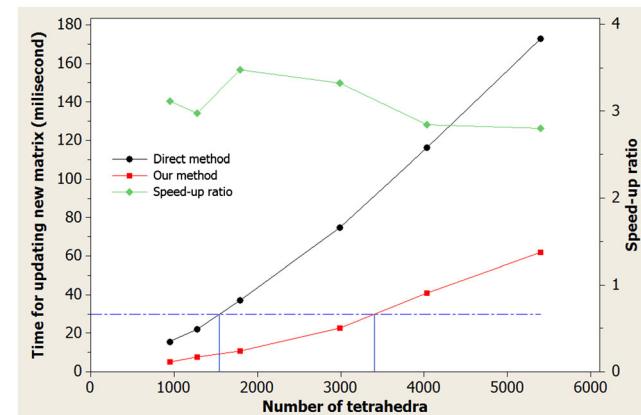


**Figure 12. Comparison of the time for node splitting and corresponding sparse matrix manipulation, using the direct method and using BCRS structure for various sizes of cut**
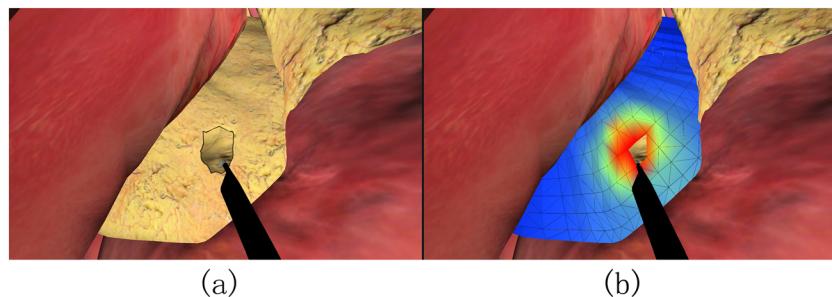
**Figure 13. Snapshot of an interactive electrosurgery simulation. Note the increased graphical detail, (a) due to the isotherm-rendering approach, and (b) compared to the tetrahedral temperature model**

which is shown to greatly reduce the computational expense of tetrahedron removal. The algorithm has been successfully incorporated into an existing surgical simulator (25).

At this point, the only tissue effect is vaporization. Other temperature-dependent tissue effects, particularly desiccation, denaturation and charring, are important (26) and will be incorporated as part of future work. In addition, we plan to incorporate other visible tissue changes, such as in colour, subsurface scattering and transparency, due to changes in temperature and deformation. Such changes would further enhance the visual fidelity of the simulator. Further, the simulator requires physical contact between the tissue and the instrument to conduct electricity, ignoring the possibility of electrical arcs through the intervening air.

As described above, our dual-mesh algorithm separates physics computations from the visual rendering procedure. The algorithm avoids the complexity of simulating the underlying physics on the locally tessellated mesh near the tool tip during electrosurgery. This, of course, comes at the cost of sacrificing accuracy of physics computation near the tool tip. We will leave the accurate computation of physics near the tool tip over the tessellated mesh as a future study.

Finally, in this work we have performed elastodynamic computations which are decoupled from the thermo-electrical simulations. Performing a fully coupled mechanical–thermal electrical simulation may improve physical realism and simulation accuracy, but will be more expensive. Hence, novel algorithms may need to be developed. This is thus left as future work. Experimental techniques are being developed to measure more accurate tissue properties for a variety of tissue types and states.

Given the current widespread use of electrosurgery and the limitations of existing electrosurgery training systems, an inexpensive and physically accurate simulator has the potential to greatly improve physician skills training. This study provides the first physically accurate electrical heating model in a real-time surgery simulator. The novel isotherm surface algorithm provides greatly improved visual detail while bypassing the computational complexity of standard remeshing approaches. These contributions combine to produce a detailed physical simulation of electrosurgery in real time.

# Acknowledgements

# References

1. Liane F, Pascal F, Daniel JB. SAGES Manual on the Fundamental Use of Surgical Energy (FUSE). Springer: New York.
2. Pearce JA. Electrosurgery. Wiley: Chapman & Hall, London.
3. Fitzgerald JEF, Malik M, Ahmed I. A single-blind controlled study of electrocautery and ultrasonic scalpel smoke plumes in laparoscopic surgery. *Surg Endosc* 2012; **26**(2): 337–342.
4. Lim YJ, Jin W, De S. On some recent advances in multimodal surgery simulation: a hybrid approach to surgical cutting and the use of video images for enhanced realism. *Presence Teleoperat Virt Environ* 2007; **16**(6): 563–583.
5. Müller M, Dorsey J, McMillan L, et al. Stable real-time deformations. In Proceedings of the ACM SIGGRAPH/Eurographics Symposium on Computer Animation, New York, 2002; 49–54.
6. Bro-Nielsen M, Cotin S. Real-time volumetric deformable models for surgery simulation using finite elements and condensation. *Comput Graph Forum* 1996; **15**(3): 57–66.
7. Dodde RE, Miller SF, Geiger JD, et al. Thermal–electric finite element analysis and experimental validation of bipolar electrosurgical cautery. *J Manuf Sci Eng* 2008; **130**(2): 021015–021015.
8. Maciel A, De S. Physics-based real time laparoscopic electrosurgery simulation. *Stud Health Technol Inform* 2008; **132**: 272–274.
9. Lu Z, Sankaranarayanan G, Deo D, et al. Towards physics-based interactive simulation of electrocautery procedures using PhysX. In IEEE Haptics Symposium, 2010; 515–518.
10. Lu Z, Arikatla VS, Chen D, et al. Real-time electrocautery simulation for laparoscopic surgical environments. *Stud Health Technol Inform* 2011; **163**: 311–316.
11. Jacob PD. Electrocautery Health and Safety Handbook of Modern Hospital Safety. CRC Press: Florida, 1999; 383–388.
12. De S, Deo D, Sankaranarayanan G, et al. A physics-driven neural networks-based simulation system (PhyNNeSS) for multimodal interactive virtual environments involving nonlinear deformable objects. *Presence (Camb)* 2011; **20**(4): 289–308.
13. Delingette H, Cotin S, Ayache N. A hybrid elastic model allowing real-time cutting, deformations and force-feedback for surgery training and simulation. In Computer Animation Proceedings, 1999; 70–81.
14. Steinemann D, Harders M, Gross M, et al. Hybrid cutting of deformable solids. In Virtual Reality Conference, 2006; 35–42.
15. Kaplan L, Uribe JW. The acute effects of radiofrequency energy in articular cartilage: an *in vitro* study. *Arthroscopy* 2000; **16**(1): 2–5.
16. Müller M, Gross M. Interactive virtual materials. In Proceedings of Graphics Interface, School of Computer Science, University of Waterloo, ON, Canada, 2004; 239–246.

17. Liu M, Gorman DG. Formulation of Rayleigh damping and its extensions. *Comput Struct* 1995; **57**(2): 277–285.
18. Cakir O, Yazici R, Cakir O. Real-time cutting simulation based on stiffness-warped FEM. In 24th International Symposium on Computer and Information Sciences (ISCIS), 2009; 721–724.
19. Pennes HH. Analysis of tissue and arterial blood temperatures in the resting human forearm. *J Appl Physiol* 1948; **1**(2): 93–122.
20. Berjano EJ. Theoretical modeling for radiofrequency ablation: state-of-the-art and challenges for the future. *Biomed Eng Online* 2006; **5**: 24.
21. Bathe KJ. Finite Element Procedures. Prentice Hall: New Jersey, 2006.
22. Pinar A, Heath MT. Improving performance of sparse matrix–vector multiplication. In Proceedings of the 1999 ACM/IEEE Conference on Supercomputing (CDROM), New York; 1999.
23. Shahnaz R, Usman A, Chughtai IR. Review of storage techniques for sparse matrices. In 9th IEEE International Multitopic Conference (INMIC), 2005; 1–7.
24. Carter FJ, Frank TG, Davies PJ, *et al*. Measurements and modelling of the compliance of human and porcine organs. *Med Image Anal* 2001; **5**(4): 231–236.
25. Sankaranarayanan G, Adair JD, Halic T, *et al*. Validation of a novel laparoscopic adjustable gastric band simulator. *Surg Endosc* 2011; **25**(4): 1012–1018.
26. Sankaranarayanan G, Resapu RR, Jones DB, *et al*. Common uses and cited complications of energy in surgery. *Surg Endosc* 2013; **27**(9): 3056–3072.
27. Bower BF. Applied Mechanics of Solids. CRC Press: Florida, 2010.